

Improved Photophysical and Photochemical Properties of Thiopheneethoxy Substituted Metallophthalocyanines on Immobilization onto Gold-speckled Silica Nanoparticles

Edith Dube, David O. Oluwole and Tebello Nyokong*

Department of Chemistry, Center for Nanotechnology Innovation, Rhodes University, Grahamstown, South Africa

Received 19 October 2017, accepted 28 November 2017, DOI: 10.1111/php.12879

ABSTRACT

This work reports on the synthesis of tetrakis-[(thiopheneethoxy) phthalocyaninato] indium(III) chloride (**3**). The photophysical behavior of complex **3** was compared to that of the Zn derivative (tetrakis-[(thiopheneethoxy) phthalocyaninato] zinc(II) (complex **2**)). The compounds were interacted with gold-speckled silica (GSS) nanoparticles via Au–S self assembly to afford the conjugates (**2**–GSS and **3**–GSS). The photophysicochemical behavior of the compounds and their conjugates were assessed. The conjugates afforded a decrease in fluorescence quantum yields and lifetimes with improved triplet and singlet oxygen quantum yields in comparison with complexes **2** and **3** alone. The complexes and their conjugates could serve as good candidates for photodynamic therapy.

INTRODUCTION

Metallophthalocyanines (MPcs) have proven to be efficacious photosensitizers (PS) for photodynamic therapy (PDT) (1). However, their selectivity and specificity toward tumor cells in comparison with healthy ones remains a daunting challenge. Consequently, efforts have been made to conjugate MPcs to nanocarriers such as nanoparticles (NPs) in order to effectively enhance their selectivity and specificity through enhanced permeability and retention (EPR) effect (1–3). NPs' marked advantage is their capability to be explored in multitask platforms (4).

Silica-based NPs (SiNPs) have shown a great promise as platforms for improved drug delivery systems due to their low toxicity, high biocompatibility, photophysical inertness, high loading capacity, ease of preparation, high surface-to-volume ratio and flexible functionalization (5,6). These properties have afforded them applications in catalysis (7), sensing (8), theranostics, diagnosis and drug delivery. In drug delivery, drug molecules (such as metallophthalocyanines, MPcs) can be encapsulated or covalently linked to SiNPs (9).

In this work, MPcs are linked to gold-speckled silica (GSS) nanoparticles. The GSS NPs have a silica core that has discontinuous, irregular gold nanodomains within the pores and on the surface of the silica matrix. The pores allow for the encapsulation of PS such as MPcs employed in this work. GSS have been used for photothermal therapy (PTT) of cancer before (10,11);

however, there are no reports in the literature of their linkage to MPcs for possible use in PDT.

PDT combines three vital components for its therapeutic activity: a PS (such as MPc), visible light and molecular oxygen, to generate a reactive oxygen species that can induce tumor cell death (12). For the efficient generation of singlet oxygen, the triplet state of MPcs should be populated. Heavy atoms in the central cavity of MPcs encourage intersystem crossing to triplet state through the heavy atom effect (13–15). In addition, Au in the NPs composite is expected to foster improved triplet quantum yield as Au is heavy atom. Enhanced triplet state quantum yields leads to improved singlet oxygen generation, as the latter is generated when the triplet state of Pc interacts with the ground state molecular oxygen.

In this work, tetrakis-[(thiopheneethoxy) phthalocyaninato] indium(III) chloride (**3**) was synthesized for the first time and its behavior compared to that of the reported Zn derivative (**2**) (16). These MPcs have a thiophene moiety which enables conjugation to GSS through Au–S self assembly. Zn and In were chosen as central metals as they are heavy atoms. The conjugation of GSS to MPcs is reported here for the first time. The MPcs, NPs (GSS) and the conjugates were characterized, and the photophysicochemical properties were studied.

MATERIALS AND METHODS

Materials. Indium(III) chloride, 1,8-diazobicyclo[5.4.0]undec-7-ene (DBU), 1-pentanol, zinc phthalocyanine (ZnPc), anthracene-9,10-bis-methylmalonate (ADMA) and 1,3-diphenylisobenzofuran (DPBF) were acquired from Sigma-Aldrich. Dimethyl sulphoxide (DMSO), dimethyl formamide (DMF) and tetrahydrofuran (THF) were acquired from Merck. A Milli-Q Water System (Millipore Corp, Bedford, MA, USA) was utilized to obtain ultra-pure water. Solvents and all other reagents obtained from commercial suppliers were used as received. For the purification processes, silica gel 60 (0.063–0.200 mm; for column chromatography) was utilized. AlPcSmix (containing a mixture of sulfonated derivatives and used as a standard for singlet oxygen quantum yields determination in water) was synthesized as reported before (17). 4-(2-(2-Thienyl)ethoxy)phthalonitrile (16), tetrakis-[(thiophene ethoxy) phthalocyaninato] Zn(II) (16), (3-aminopropyl)triethoxysilane (APTES) functionalized silica nanoparticles (SiNPs-APTES) (18) and gold nanoparticle seeds (19) were synthesized as reported in the literatures.

Equipment. Infrared spectra were obtained using a Bruker ALPHA FT–IR spectrometer with universal attenuated total reflectance (ATR) sampling accessory. Elemental analyses were performed using a Vario-Elementar Microcube ELIII. Mass spectra and data were obtained using a Bruker AutoFLEX III Smart-beam TOF/TOF mass spectrometer with α -cyano-4-hydrocinnamic acid as the matrix. ^1H and ^{13}C NMR spectra were obtained using a Bruker AVANCE II 600 MHz NMR spectrometer

*Corresponding author email: t.nyokong@ru.ac.za (Tebello Nyokong)
© 2017 The American Society of Photobiology

with tetramethylsilane (TMS) as an internal reference. X-ray powder diffraction patterns were acquired using a Cu K α radiation (1.5405 Å, nickel filter), on a Bruker D8 Discover equipped with a proportional counter and the data were processed using the Eva (evaluation curve fitting) software. Transmission electron microscope (TEM), ZEISS LIBRA model 120 operated at 90 kV was used to assess the morphologies of the NPs and their conjugates, and iTEM software was used for TEM micrographs processing. Qualitative determination of the elemental compositions of the NPs and the conjugates was performed using energy dispersive X-ray spectroscopy (EDX), INCA PENTA FET coupled to the VAGA TESCAME operated at 20 kV accelerating voltage. A Shimadzu UV-2550 spectrophotometer was used to measure ground state electronic absorption. A Varian Eclipse spectrofluorimeter utilizing a 360- to 1100-nm filter was used to determine fluorescence excitation and emission. Excitation spectra were recorded using the Q-band of the emission spectra. A time correlated single photon counting (TCSPC) setup (FluoTime 300, Picoquant GmbH) with a diode laser (LDH-P-670, Picoquant GmbH, 20 MHz repetition rate, 44 ps pulse width) was used to measure fluorescence lifetimes, and details have been provided before (20).

For the determination of triplet quantum yields, a laser flash photolysis system was used, with excitation pulses being produced using a tunable laser system consisting of an Nd:YAG laser (355 nm, 135 mJ/4–6 ns) pumping an optical parametric oscillator (OPO, 30 mJ/3–5 ns) with a wavelength range of 420–2300 nm (NT-342B, Ekspla), as reported before (21).

Irradiation for singlet oxygen quantum yield was performed using a General Electric projector lamp (300 W) as described in the literature (22). A 600-nm glass cutoff filter (Schott) and water were used to filter off ultraviolet and infrared radiations, respectively. Interference filter (Intor, 670 nm with band a width of 40 nm) was additionally placed in the light path before the sample. Light intensity was measured with a POWER MAX 5100 (Molelectron detector incorporated) power meter and was found to be 4.3×10^{15} photons $\text{cm}^{-2} \text{s}^{-1}$.

Magnetic circular dichroism (MCD) spectra were acquired using a Chirascan plus spectrodichromometer equipped with a 1 T (tesla) permanent magnet using both the parallel and antiparallel fields. The conventions of Piepho and Schatz are used to describe the sign of the MCD signal and the Faraday terms (23).

An AXIS Ultra DLD, with Al (monochromatic) anode equipped with a charge neutralizer, supplied by Kratos Analytical was used to acquire X-ray photoelectron spectroscopy (XPS) data. The following parameters were used: The emission was 10 mA, the anode (HT) was 15 kV and the operating pressure below 5×10^{-9} torr. A hybrid lens was used, and resolution to acquire scans was at 160 eV pass energy in slot mode. The center used for the scans was at 520 eV with a width of 1205 eV, steps at 1 eV and dwell time at 100 ms as. The high resolution scans were acquired using 80 eV pass energy in slot mode.

Syntheses.

Complex 1. The synthesis of the H₂Pc (metal-free phthalocyanine) is as follows: 4-(2-(2-thienyl)ethoxy) phthalonitrile (0.58 g, 2.28 mmol), was dissolved in dry 1-pentanol (4 mL), in the presence of DBU (0.3 mL, mmol). The reaction mixture was refluxed at ~140°C for 6 h with constant stirring under nitrogen atmosphere. On cooling the reaction mixture to room temperature, methanol was added to the crude product and centrifuged. The isolation and purification was repeated successively until a pure metal free compound was obtained (H₂Pc), complex 1.

Yield: 0.45 g (77%). IR [$\nu_{\text{max}}/\text{cm}^{-1}$]: 3073(Ar-H), 2923 (C-H stretch), 1654, 1600 (C = C), 1513, 1352, 1226 (Ar-O-Ar). UV/Vis (DMSO), λ_{max} nm: 706, 673, 645, 616, 392, 343. ¹H NMR (600 MHz, DMSO) δ 8.95 (d, J = 8.12 Hz, 3H, Ar-H), 8.54 (d, J = 6.62 Hz, 3H, Ar-H), 7.61–7.04 (m, 18H, Ar-H), 4.72 (t, J = 4.88 Hz, 8H, CH₂), 4.32 (s, 2H, NH), 3.59 (t, J = 5.67 Hz, 8H, CH₂). ¹³C NMR (600 MHz, DMSO) δ 169.93, 161.87, 141.17–103.30, 69.45, 30.95–29.52. Anal. Calc. for (C₅₆H₄₂N₈O₄S₄): C, 65.99; H, 4.15; N, 10.99; S, 12.58. Found: C, 66.54; H, 3.98; N, 10.78; S, 13.03. MS (MALDI-TOF) m/z : Calcd: 1019.24; Found: 1019.30 [M]⁺.

Complex 3. The conversion of the H₂Pc to an MPc was achieved by mixing the H₂Pc (0.20 g, 1.96 mmol) with indium chloride (0.20 g, 0.90 mmol) in 5 mL chloronaphthalene and heating at ~100°C for 5 h. Upon cooling the reaction mixture to room temperature,

methanol was added and the resulting precipitate centrifuged, and washed several times with methanol. The product (complex 3) was dried under vacuum and purified by column chromatography (silica gel, THF-methanol, 9:1).

Tetrakis-[(thiophineethoxy) phthalocyaninato] indium(III) chloride (**3**): Yield: 0.15 g (75%). IR [$\nu_{\text{max}}/\text{cm}^{-1}$]: 3069(Ar-H), 2921 (C-H stretch), 1599 (C = C), 1515, 1348, 1228 (Ar-O-Ar). UV/Vis (DMSO), λ_{max} nm (log ϵ): 696 (4.89), 627 (4.43), 332 (4.55). ¹H NMR (600 MHz, DMSO) δ 8.99 (d, J = 7.83 Hz, 3H, Ar-H), 8.54 (d, J = 6.69 Hz, 3H, Ar-H), 7.67–7.08 (m, 18H, Ar-H), 4.75 (t, J = 5.42 Hz, 8H, CH₂), 3.52 (t, J = 5.99 Hz, 8H, CH₂). ¹³C NMR (600 MHz, DMSO) δ 169.18, 161.95, 141.03–103.39, 69.50, 30.05–29.90. Anal. Calc. for (C₅₆H₄₀ClInN₈O₄S₄): C, 57.61; H, 3.45; N, 9.60; S, 10.99. Found: C, 57.94; H, 3.63; N, 9.51; S, 10.69. MS (MALDI-TOF) m/z : Calcd: 1167.50; Found: 1167.26 [M]⁺.

Gold-speckled silica (GSS) nanoparticles. For the attachment of gold seeds onto functionalized silica cores, 40 mg of APTES functionalized silica nanoparticles were dispersed in THF and placed in a 150 mL flask with an excess of gold seeds. The mixture was stirred gently for 5 min and then allowed to stand for 2 h. The mixture was then centrifuged, washed with water and the gold decorated SiNPs (GSS) were dried.

Covalent linkage of complexes 2 and 3 to GSS (Scheme 2). The phthalocyanine–GSS conjugates were synthesized as follows: complex 2 (0.02 g, 0.018 mmol) or complex 3 (0.02 g, 0.019 mmol) were dissolved in dry DMF (2 mL). GSS (0.05 g) were added and the reaction mixture was stirred for 24 h at room temperature. Following literature methods (24) the mixture was centrifuged at 2465 g for 10 min to separate the MPc-GSS (at the bottom) and unbound MPc (supernatant). MPc-GSS conjugates were washed (using ethanol) with centrifuging until the supernatant was clear, to ascertain removal of any residual free MPc, then they were allowed to dry in the fume hood. The conjugates are represented as 2-GSS and 3-GSS. The conjugates were then suspended in DMSO for future use.

Photophysical studies. Triplet (Φ_T) and fluorescence (Φ_F) quantum yields of complexes 2, 3 and their conjugates were determined in DMSO using comparative methods described before in the literature (25–27). Unsubstituted ZnPc in DMSO was used as a standard with Φ_T = 0.65 (26) and Φ_F = 0.20 (27). Before measurements, all solutions for triplet state studies were de-aerated with argon for 15 min.

Singlet oxygen quantum yield (Φ_{Δ}) determination was conducted under ambient conditions using DPBF as a singlet oxygen quencher in DMSO (and ADMA in water) and equations described before (28–30). Unsubstituted ZnPc was used as a standard in DMSO ($\Phi_{\Delta(\text{Std})}$ = 0.67 in DMSO) (28), and AlPcSmix was employed as a standard in aqueous media ($\Phi_{\Delta(\text{Std})}$ = 0.42 (30)). Complexes 2 and 3 and their conjugates with GSS are not soluble in water; hence, for studies in water they were first dissolved in 50 μL DMSO and then diluted with water to 10 mL. The aqueous media is important for future biological applications. The absorbances of DPBF or ADMA were spectroscopically monitored at 417 nm or 380 nm, respectively, at a predetermined time course.

RESULTS

Synthesis and characterization of complexes 2 and 3

Scheme 1 shows the synthetic pathway for complex 3. The complex was synthesized in two steps; the first step was the synthesis of the unmetallated Pc (H₂Pc) and the second step involves the metallation of the H₂Pc. Tetrakis-(thiophineethoxy) phthalocyanine (H₂Pc) was synthesized by cyclocondensation of 4-(2-(2-thienyl)ethoxy) phthalonitrile in the presence of DBU and 1-pentanol. The H₂Pc was then metallated using an indium metal salt. The disappearance of the C \equiv N peak of the phthalonitrile at 2228 cm^{-1} observed in the FT-IR spectra (Fig. 1) confirmed the formation of complex 3. The ¹H NMR spectrum for complex 3 displayed aromatic ring proton peaks between 8.99 and 8.54 ppm and between 7.67 and 7.08 ppm. The protons of the CH₂ of the ethoxy groups were observed between 4.75 and 3.52 ppm (see Figure S1). Peak integration

gave the expected total number of protons, confirming the relative purity of the complex. The ^{13}C NMR, on the other hand, displayed aromatic ring proton peaks between 169.18 and 161.95 ppm and between 141.03 and 103.39 ppm. The CH_2 protons of the ethoxy groups were observed at 69.50 ppm and between 30.05 and 29.90 ppm (Figure S2). It should be noted, however, that as the MPC is symmetrical, some peaks are overlapping. Mass spectral data (Figure S3) and elemental analyses were in agreement with the proposed structure in Scheme 1.

The absorption spectra for both complexes **2** and **3** in DMSO (Fig. 2) show their monomeric behavior as evidenced by a narrow, single Q-band at 682 and 695 nm, for complexes **2** and **3**, respectively (Table 1), which is typical for metalated phthalocyanines with degenerate D_{4h} symmetry (31). The red shift in the Q-band of complex **3** compared to **2** can be attributed to the nonplanar effect of the indium(III) ion, with a relatively bigger atomic radius than the zinc(II) as the central metal ion in the Pc cavity (32,33).

Magnetic circular dichroism gives information about state degeneracies, which cannot be obtained from the UV-visible absorption spectrum alone (34). The MCD spectra of complexes **2** (Fig. 3) and **3** (Figure S4) are characteristic of monomeric MPCs, as intense A_1 terms were observed in the Q and B-band regions with cross-over points at 682 nm and 348 nm, respectively, for complex **2**; 695 nm and 353 nm, respectively, for complex **3**, as would be expected for transitions to degenerate or near degenerate excited states (34). Thus, using MCD spectroscopy, 682 nm and 348 nm pseudo- A_1 terms can be clearly assigned to the Q and B transitions of complex **2**, and 695 nm

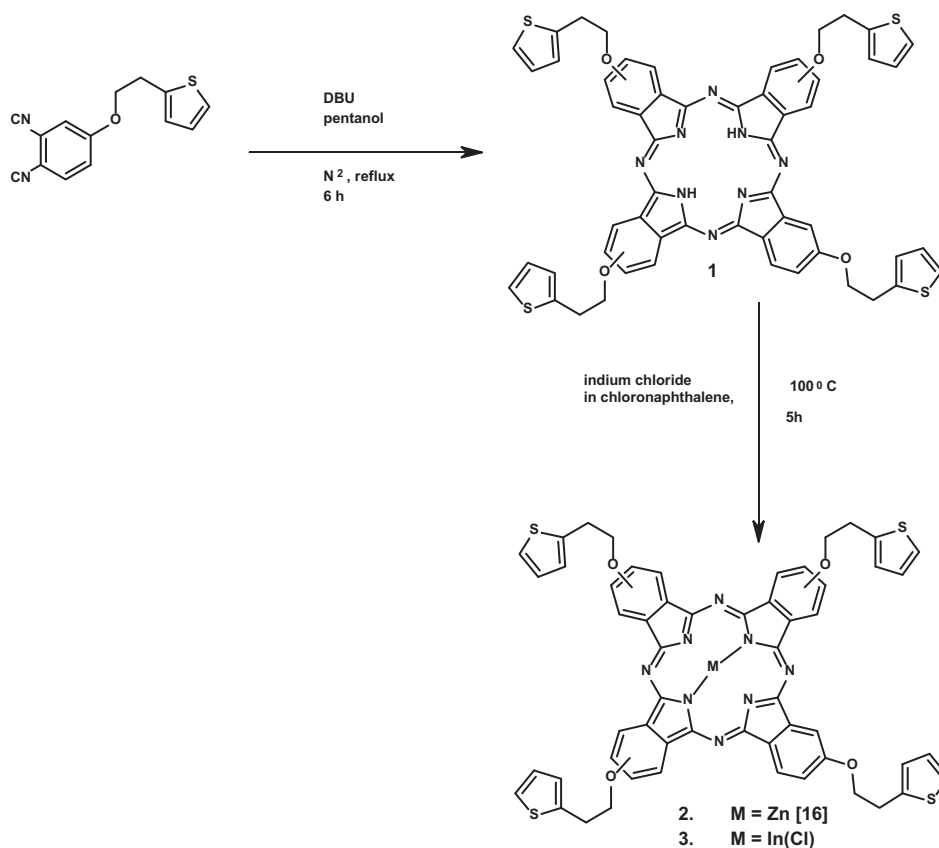
and 353 nm for complex **3**, in accordance with Gouterman's four-orbital model (35).

The ground state absorption, excitation and emission spectra for complex **2** in DMSO are shown in Fig. 4, as an example. The ground state absorption and fluorescence excitation for all complexes were mirror images of the emission spectra. The closeness of the wavelength of the Q-band absorption to the Q-band maxima of the excitation spectra shows that the nuclear configurations of the ground and excited states are similar (not affected by excitation) and that the complexes in DMSO are not aggregated.

Synthesis and characterization of the conjugates

Scheme 2 shows the linking of the Pcs to the nanoparticles.

FT-IR spectra. FT-IR spectroscopy (Fig. 1) was employed to assess the functional groups present on the NPs and the conjugates. The gold-speckled silica nanoparticles (GSS) showed two distinct bands at 792 cm^{-1} , corresponding to the primary amine from the capping ligand (APTES) and 1056 cm^{-1} corresponding to siloxane band (Si-O-Si). The conjugates (**3**-GSS as an example, (Fig. 1b) also showed these two distinct bands in addition to peaks at 1521 cm^{-1} and 1603 cm^{-1} (C = C) which might be due to the presence of the MPC complexes on conjugation to NPs as similar bands were observed in the complexes alone (Fig. 1c) at 1515 cm^{-1} and 1599 cm^{-1} . The siloxane bands dominated the spectra of GSS and its conjugates making it difficult to see other bands, as a result FTIR cannot be



Scheme 1. Synthesis of tetrakis-(thiophineethoxy) phthalocyaninato indium(II) chloride (complex **3**).

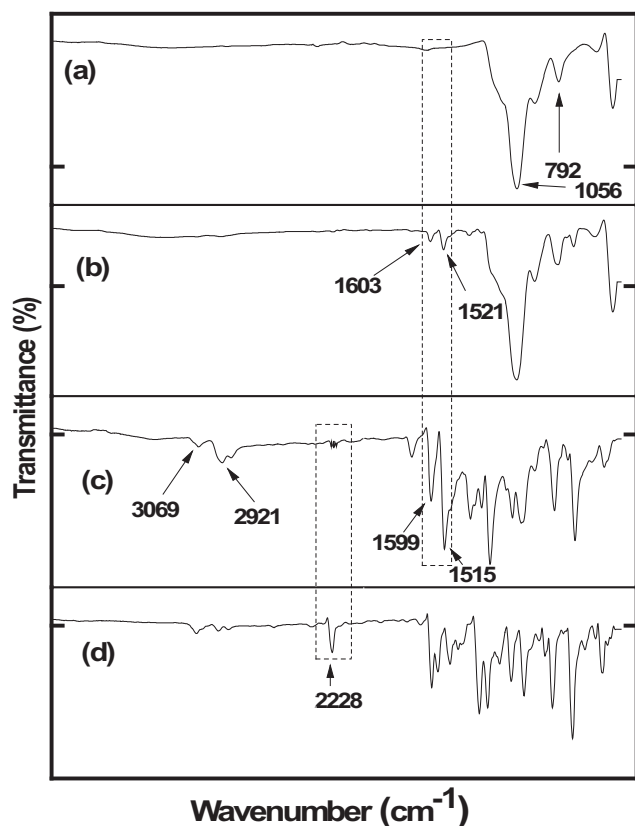


Figure 1. FT-IR spectra of (a) GSS, (b) 3-GSS, (c) complex 3 and (d) 4-(2-(2-thienyl)ethoxy) phthalonitrile.

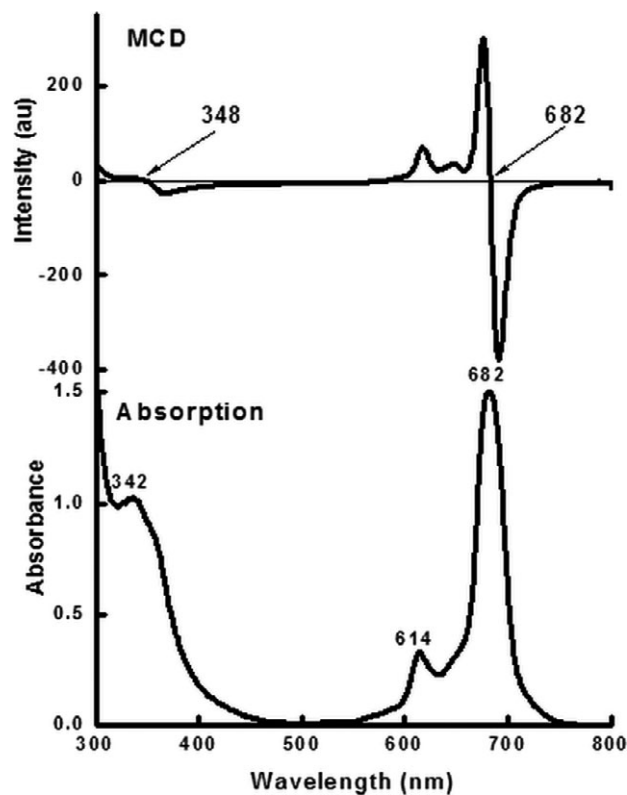


Figure 3. Absorption and MCD spectra of complex 2 in DMSO.

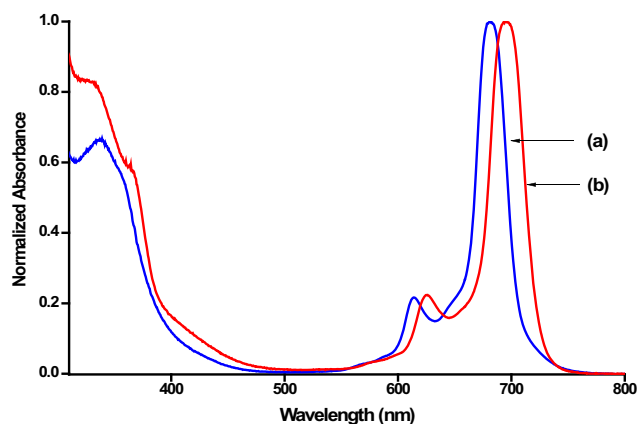


Figure 2. Absorption spectra of (a) complex 2 and (b) complex 3; solvent = DMSO.

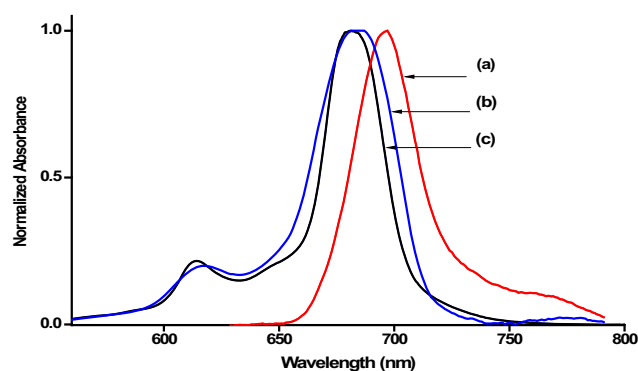
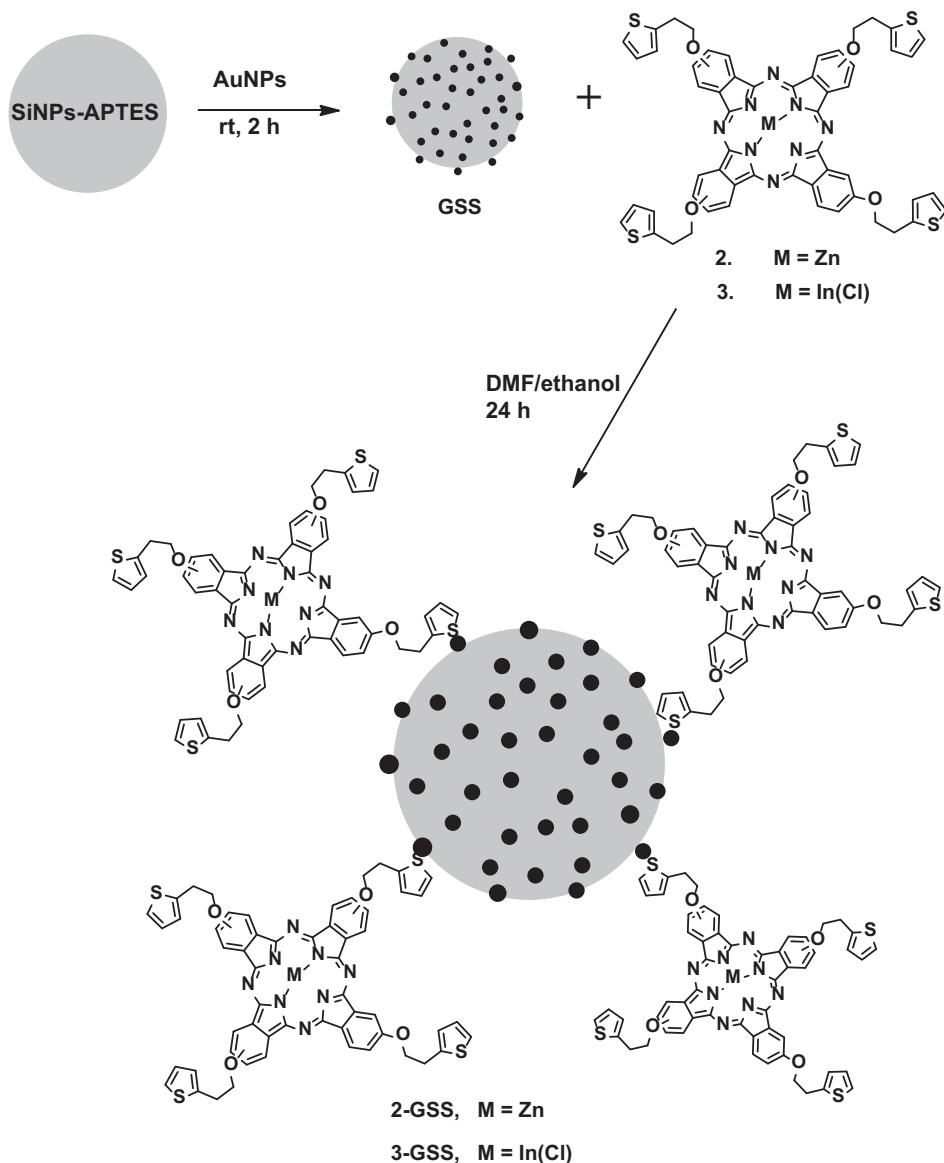


Figure 4. (a) Emission, (b) excitation and (c) absorption spectra of complex 2 (excitation = 610 nm, solvent = DMSO).

Table 1. Photophysical parameters of complexes 2 and 3 and their conjugates in DMSO.

Samples	Size (nm)*	$\lambda_{\text{abs}}(\text{nm})^\dagger$	Pc loading ($\mu\text{g}/\text{mg}$)	$\Phi_{\text{F}}(\pm 0.01)$	$\tau_{\text{F}}(\text{ns})(\pm 0.03)$	$\Phi_{\text{T}}(\pm 0.02)$	$\tau_{\text{T}}(\mu\text{s})(\pm 2)$	$\Phi_{\Delta}^\ddagger(\pm 0.01)$
2	—	682 (695)	—	0.15	3.12	0.47	306	0.33 (0.07)
2-GSS	81.7 (5.42)	681 (694)	51	0.10	3.03	0.64	242	0.54 (0.10)
3	—	695 (712)	—	0.02	0.88	0.60	225	0.42 (0.08)
3-GSS	82.3 (6.43)	697 (711)	49	0.01	2.83	0.72	49	0.67 (0.13)

*Numbers in brackets are for Au speckles only. The particle size for GSS alone is 78.4 nm, and for Au speckles alone is 4.51 nm. ‡ Numbers in brackets are the values in water (with 0.5% DMSO).



Scheme 2. Synthetic pathways for GSS, 2-GSS and 3-GSS.

conclusively used to confirm the conjugation of the complexes to the gold-speckled SiNPs. XPS was then applied below to confirm doping.

UV-vis absorption of the complexes and conjugates. An overlay of the normalized absorption spectra of GSS with complex **2** (Fig. 5A), complex **3** (Fig. 5B), and their conjugates is shown. GSS displayed a maximum absorption at 599 nm which is attributed to the surface plasmon resonance (SPR) band of the nanogold on silica surfaces which is more red-shifted compared to the reported (12) values for GSS, probably due to the larger size of GSS. Upon conjugation of complexes **2** and **3** to GSS, an enhancement in absorption between the vibronic band and the B-band was observed showing the presence of nanoparticles in the conjugate. In water (Fig. 6), the complexes and their conjugates show broad bands due to aggregation typical of Pcs in aqueous solution (36) resulting from π - π stacking interaction of the aromatic rings of Pcs.

The loading of complexes **2** and **3** onto the nanoparticles was investigated following literature methods (24). This involves

dissolving the same mass of the Pc alone and the conjugate in an equal volume of solvent and comparing the Q-band absorbance intensity of the Pc in the conjugate with that of the initial Pc before the conjugation. A decrease in intensity was observed in the conjugates compared to the Pc. The loadings of Pc onto nanoparticles are listed in Table 1. There was not much difference in loading (Table 1), with **2-GSS** having a slightly higher loading than **3-GSS**.

XRD studies. Figure 7 shows the powder XRD patterns for GSS, **2-GSS** and complex **2**, as examples. Broadness in XRD pattern for complex **2** alone (Fig. 7C) is known to portray the amorphous nature of phthalocyanines as described before (37). Sharp peaks at $2\theta = 38.3^\circ$, 44.2° , 64.6° , 77.2° and 81.1° , as observed for GSS (Fig. 7A) and the conjugates (Fig. 7B, **2-GSS** as an example) show crystallinity. These peaks were assigned to the 111, 200, 220, 311 and 222 planes, respectively, corresponding to the face centered-cubic structures of metallic gold (38). The broad peak at $2\theta = 10^\circ$ to 22° for GSS (Fig. 7A) and the

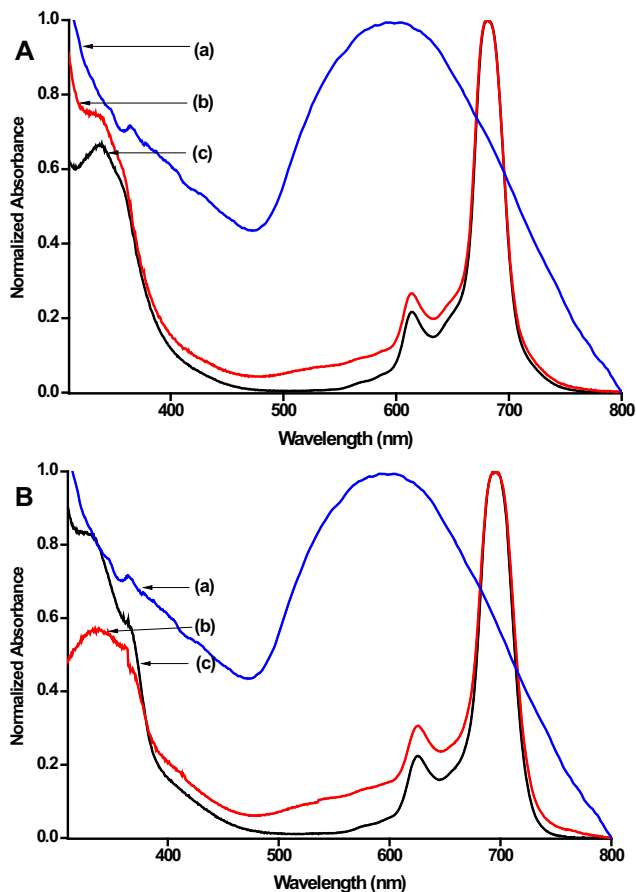


Figure 5. (A) Absorption spectra of (a) GSS, (b) 2-GSS and (c) complex 2. (B) Absorption spectra of (a) GSS, (b) 3-GSS and (c) complex 3. Solvent = DMSO.

conjugates (Fig. 7B, 2-GSS as an example) is attributed to the amorphous nature of SiNPs in GSS alone and the phthalocyanine in addition to silica in the conjugates.

Size estimates from XRD were obtained only for the gold speckles on silica and after conjugation using the Debye–Scherrer (39) Eq. 1, by focusing on the (111) peaks:

$$d = \frac{k\lambda}{\beta \cos \theta} \quad (1)$$

where λ is the wavelength of the X-ray source (1.5405 Å), k is an empirical constant equal to 0.9, β is the full width at half maximum of the diffraction peak and θ is the angular position. The sizes were estimated to 4.51 nm for gold speckles on GSS, 5.42 nm for gold speckles after conjugation in 2-GSS and 6.43 nm for gold speckles after conjugation in 3-GSS, Table 1.

Transmission electron microscopy (TEM). Figure 8 shows the TEM micrographs of the NPs and their conjugates. The SiNPs are spherical and aggregated (Fig. 8A). The micrographs for GSS, Fig. 8B, show discontinuous and random deposits of nano-gold (as shown by small darker spheres) on silica surfaces, confirming the formation of gold-speckled SiNPs (GSS). The aggregation was observed for GSS before (Fig. 8B) and

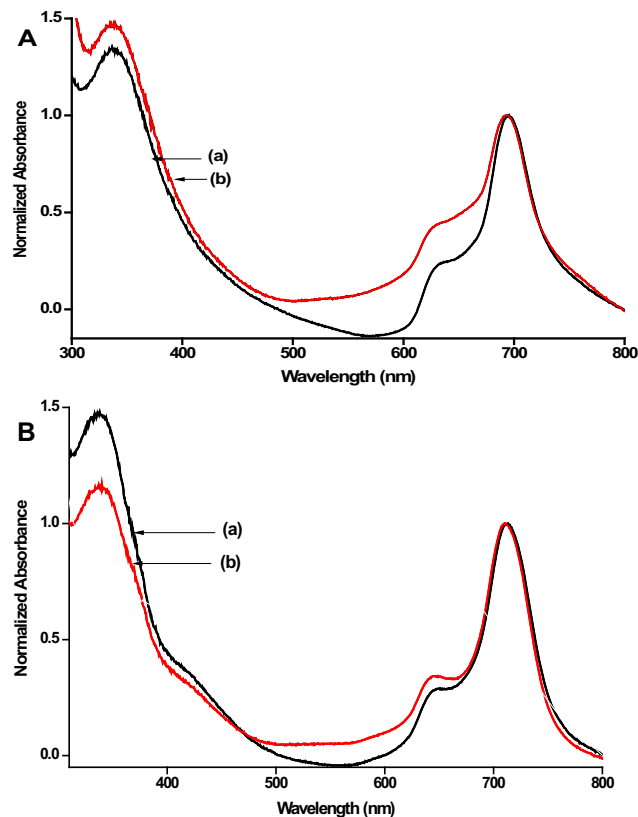


Figure 6. (A) Absorption spectra of (a) complex 2 and (b) 2-GSS. (B) Absorption spectra of (a) complex 3 and (b) 3-GSS. Solvent = water (with 0.5% DMSO).

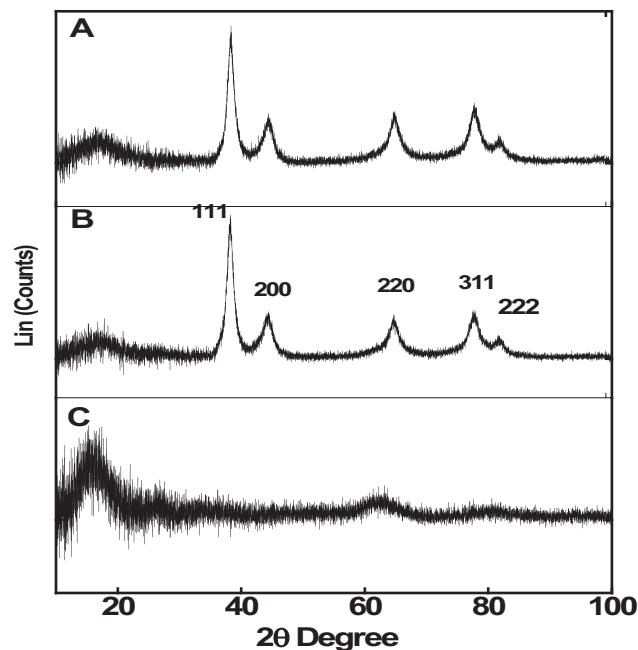


Figure 7. XRD diffractograms for (A) GSS, (B) 2-GSS and (C) complex 2.

increased on linkage to the complexes (Fig. 8C and 8D). Increased aggregation in the conjugates is possible due to likely π - π stacking that can occur between the Pcs on adjacent NPs.

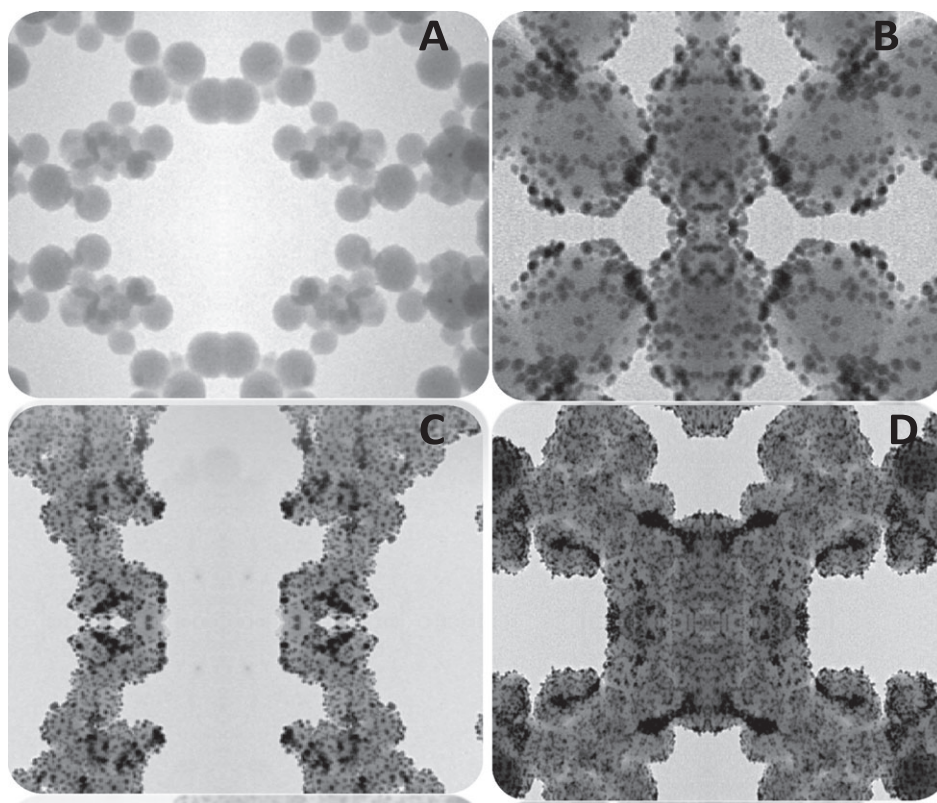


Figure 8. Representative TEM micrographs for (A) SiNPs-APTES, (B) GSS, (C) 2-GSS and (D) 3-GSS.

Pcs are known for their π - π stacking to form H aggregates (36). The average size of the NPs was estimated to 78.4 nm for GSS, 81.7 nm for 2-GSS and 82.3 nm for 3-GSS (Table 1).

EDX spectra. The energy dispersive X-ray spectrometer (EDX), shown in Fig. 9, was used for qualitative determination of the elemental composition of complexes and their conjugates. The

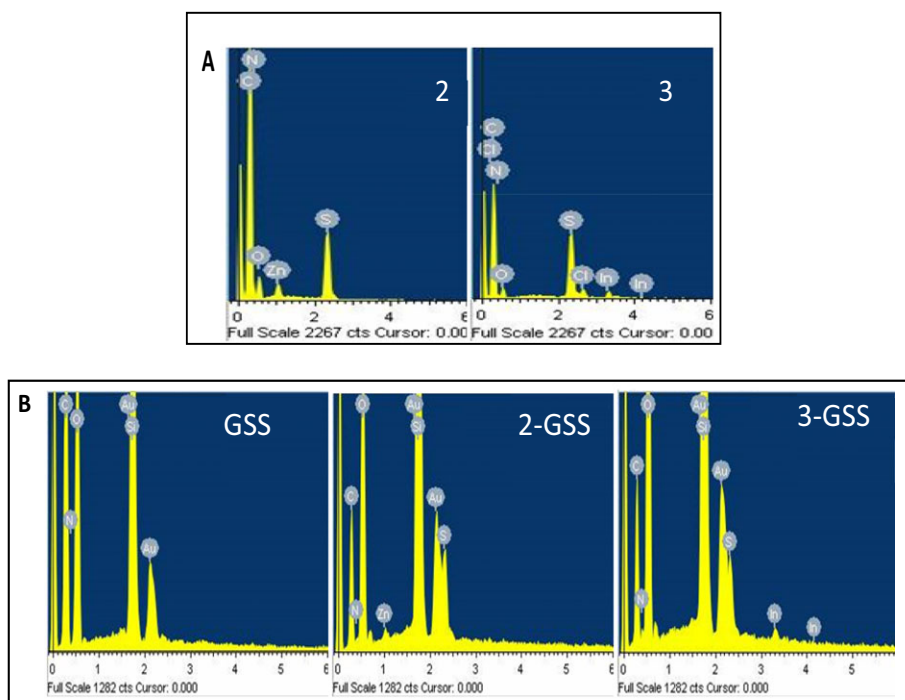


Figure 9. EDX spectra of (A) complexes 2 and 3 and (B) GSS, 2-GSS and 3-GSS.

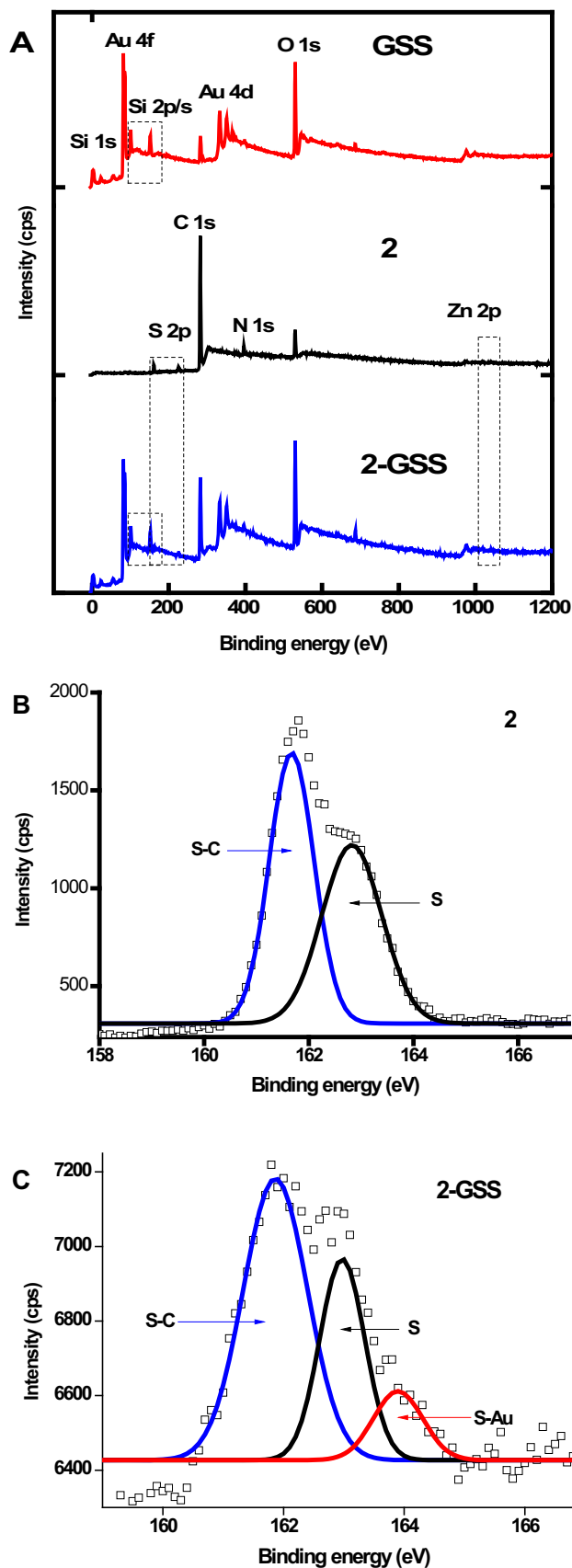


Figure 10. XPS spectra: (A) survey spectra for GSS, complex 2 and 2-GSS; (B) and (C) high resolution S2p spectra for complex 2 and 2-GSS, respectively.

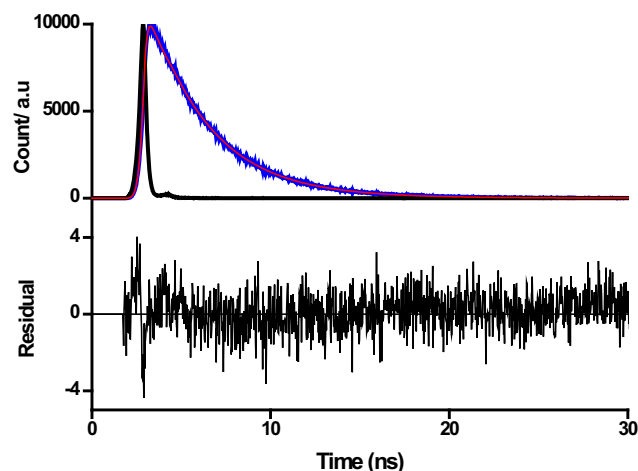


Figure 11. Fluorescence decay (blue), χ^2 fitting (red) and IRF (black) curves for 2-GSS in DMSO.

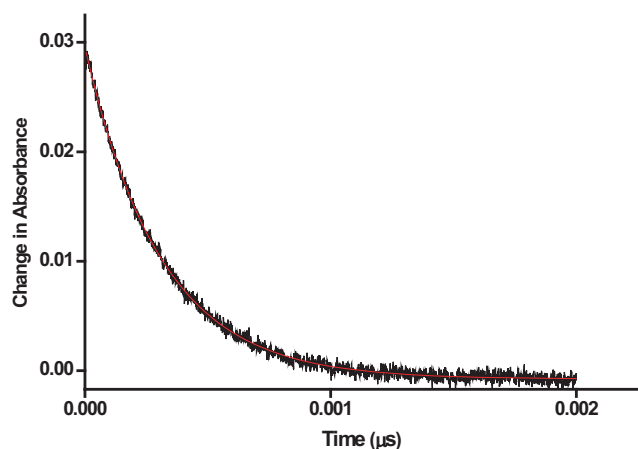


Figure 12. Triplet absorption decay curve (black) and fitting (red) for 2-GSS in DMSO.

spectra of complexes 2 and 3 showed the presence of C, N, S and O in addition to Zn for complex 2 and, In and Cl for complex 3, as expected for metalphthalocyanines. GSS and the conjugates (2-GSS and 3-GSS) showed the presence of Si, Au, C, N and O. Additionally, 2-GSS showed the presence of S and Zn, while 3-GSS showed S, In and Cl.

XPS Spectra. The interaction between AuNPs and complex 2 (as an example) was confirmed using XPS analysis. The XPS survey spectra (Fig. 10A) exhibited the expected elements and their respective binding energies. GSS displayed Si (0.99 eV, 102.5 eV and 302.9 eV), Au (84.1 eV, 339.9 eV and 353.0 eV), C (285 eV), N (396 eV) and O (532 eV). Complex 2 exhibited S (163 eV), C (285 eV), N (396 eV), O (532 eV) and Zn (1022 eV), while the conjugates (2-GSS as an example) displayed similar trends as complex 2, but with additional elements, Au (84.3 eV, 337.6 eV and 352.9 eV) and Si (1.01 eV, 102.8 eV and 303.2 eV) from GSS. The high-resolution analysis was employed to show the possible linkage of the MPc complexes to GSS. The S2p peak for complex 2 alone (Fig. 10B) showed two deconvoluted peaks attributed to S-C (161.7 eV)

and S (162.9 eV), while the conjugates (Fig. 10C, 2-GSS as an example) displayed three peaks attributed to S-C (161.9 eV), S (163.0 eV) and S-Au (164.0 eV). The S-Au peak indicates the successful linkage of complexes to GSS via a S-Au.

Photophysicochemical parameters

A comparison of the fluorescence quantum yields (Φ_F) and lifetimes (τ_F), triplet quantum yields (Φ_T) and lifetimes (τ_T), and singlet oxygen quantum yields (Φ_Δ) of complexes **2** and **3** alone, and their conjugates using DMSO (and in some cases water in brackets) is displayed in Table 1.

Fluorescence quantum yields (Φ_F) and lifetimes (τ_F). Figure 11 shows a typical fluorescence decay curve for 2-GSS as an example. A single fluorescence lifetime was obtained for complexes **2** and **3** alone and 2-GSS, while 3-GSS displayed two fluorescence lifetimes (only the average is shown in Table 1), possibly due to different orientations of the phthalocyanines on the NPs. Complex **3** and its conjugate displayed lower fluorescence quantum yields than complex **2** and its conjugate as complex **3** has indium, a heavier atom than zinc in its central cavity. A decrease in the fluorescence quantum yields of the complexes on conjugation to NPs demonstrates significant quenching of the excited singlet state of the complexes which could be attributed to the presence of gold, another heavy atom. As earlier stated, heavy atoms are known to encourage intersystem crossing to the triplet state through spin orbit coupling (14), thereby resulting in a decreased fluorescence quantum yield.

Triplet quantum yields (Φ_T) and lifetimes (τ_T). Triplet quantum yields (Φ_T) give an indication of the fraction of absorbing molecules that undergo intersystem crossing to the excited triplet state. Figure 12 shows the triplet decay curves for 2-GSS in DMSO, as an example. The values obtained for Φ_T and τ_T are shown in Table 1. As fluorescence and triplet state are two competing states where increase in triplet quantum yield is often expected to be accompanied by decrease fluorescence quantum yield. The Φ_T value for complex **3** was found to be higher compared to complex **2**, as indium promotes intersystem crossing to triplet state more than zinc as earlier stated. The triplet quantum yields increased for the conjugates as compared to the Pcs alone due to the presence of a heavy atom, gold in the conjugates. As expected, the high Φ_T was associated with a decrease in triplet lifetimes.

Singlet oxygen quantum yields. The singlet oxygen quantum yield (Φ_Δ) is dependent on the corresponding triplet quantum yield (Φ_T) of the photosensitizer, as the interaction of the triplet state of photosensitizer with the ground state molecular oxygen determines the efficiency of energy transfer from the photosensitizer to molecular oxygen (40,41). As expected, the highly populated triplet state of complex **3** compared to complex **2** gave a higher Φ_Δ . By the same principle, the conjugates gave higher Φ_Δ than Pcs alone as shown in Table 1. Figure 13 shows the decay curves of singlet oxygen quenchers (DPBF in DMSO, Fig. 13A and ADMA in water, Fig. 13B) upon irradiation of the complexes and their respective conjugates at the Q-band. As shown in Fig. 13, DPBF and ADMA degraded with time, with no significant decrease in the Q-bands, an indication of the stability of the complexes and conjugates during the irradiation

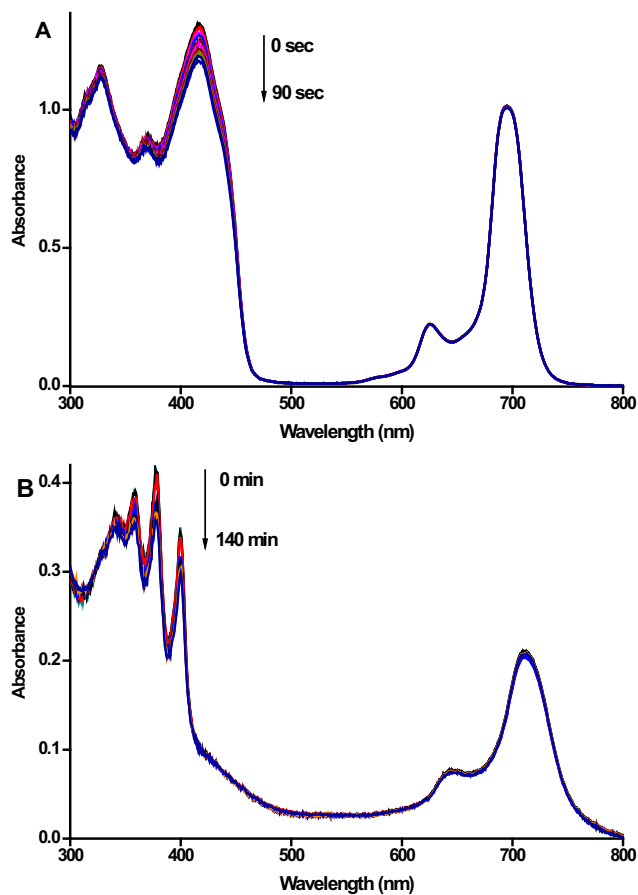


Figure 13. UV–visible spectral changes observed during the degradation of (A) DPBF in the presence of complex **3** in DMSO and (B) ADMA in the presence of 3-GSS in water (with 0.5% DMSO).

period. Water is known to quench the singlet state (27) as Pcs aggregate as shown by the broadening of Q-band; thus, values in water are low (Table 1).

CONCLUSION

In this work, we report on the synthesis of tetrakis-[(thiophineethoxy) phthalocyaninato] indium(II) chloride (complex **3**) which was characterized using FTIR, UV–vis, NMR, MALDI-TOF mass spectroscopies and elemental analyses. The photo-physical behavior of complex **3** was compared to that of the Zn derivative (tetrakis-[(thiophineethoxy) phthalocyaninato] zinc(II) (complex **2**)). The MPcs were subsequently linked to gold-speckled silica nanoparticles (GSS), and their conjugates were characterized using XRD, XPS, TEM, UV/vis, FT-IR spectrometer and EDX. The photophysicochemical behavior of the complexes and their conjugates were also studied. The conjugates displayed improved triplet and singlet quantum yields than the complexes alone.

Acknowledgements—This work was supported by the Department of Science and Technology (DST) Innovation and National Research Foundation (NRF), South Africa through DST/NRF South African Research Chairs Initiative for Professor of Medicinal Chemistry and Nanotechnology (UID 62620) as well as Rhodes University.

SUPPORTING INFORMATION

Additional Supporting Information may be found in the online version of this article:

Figure S1. ¹H NMR spectra of compounds **1** and **3**.

Figure S2. ¹³C NMR spectra of compounds **1** and **3**.

Figure S3. MS (Maldi-TOF) of compounds **1** and **3**.

Figure S4. Absorption and MCD spectra of complex **3** in DMSO.

REFERENCES

- Calixto, G. M., J. Bernegossi, L. M. de Freitas, C. R. Fontana and M. Chorilli (2016) Nanotechnology-based drug delivery systems for photodynamic therapy of cancer: A review. *Molecules* **21**(3), 342. 1–18.
- Wieder, M. E., D. C. Hone, M. J. Cook, M. M. Handsley, J. Gavrilovic and D. A. Russell (2006) Intracellular photodynamic therapy with photosensitizer-nanoparticle conjugates: Cancer therapy using a 'Trojan horse'. *Photochem. Photobiol. Sci.* **5**, 727–734.
- Roy, I., T. Y. Ohulchansky, H. E. Pudavar, E. J. Bergey, A. R. Oseroff, J. Morgan, T. J. Dougherty and P. N. Prasad (2003) Ceramic-based nanoparticles entrapping water-insoluble photosensitizing anticancer drugs: A novel drug-carrier system for photodynamic therapy. *J. Am. Chem. Soc.* **125**, 7860–7865.
- Couleaud, P., V. Morosini, C. Frochot, S. Richeter, L. Raehm and J. O. Durand (2010) Silica-based nanoparticles for photodynamic therapy applications. *Nanoscale* **2**, 1083–1095.
- Slowing, I. I., J. L. Vivero-Escoto, B. G. Trewyn and V. S. Y. Lin (2010) Mesoporous silica nanoparticles: Structural design and applications. *J. Mater. Chem.* **20**, 7924–7937.
- Hoshikawa, Y., H. Yabe, A. Nomura, T. Yamaki, A. Shimojima and T. Okubo (2010) Mesoporous silica nanoparticles with remarkable stability and dispersibility for antireflective coatings. *Chem. Mater.* **22**, 12–14.
- Huh, S., H. T. Chen, J. W. Wiench, M. Pruski and V. S. Y. Lin (2005) Cooperative catalysis by general acid and base bifunctionalized mesoporous silica nanospheres. *Angew. Chem. Int. Ed. Engl.* **44**, 1826–1830.
- Lei, J., L. Wang and J. Zhang (2010) Ratiometric pH sensor based on mesoporous silica nanoparticles and Foerster resonance energy transfer. *Chem. Commun.* **46**, 8445–8447.
- Rampazzo, E., L. Prodi, L. Petrizza, N. Zacchero (2016) Light-responsive nanostructured systems for applications in nanomedicine. In *Topics in Current Chemistry*, Vol. **370** (Edited by S. Sortino), pp. 3–28. Springer, Berlin, Germany.
- Sharma, P., S. C. Brown, A. Singh, N. Iwakuma, G. Pyrgiotakis, V. Krishna, J. A. Knapik, K. Barr, B. M. Moudgil and S. R. Grobmyer (2010) Near-infrared absorbing and luminescent gold speckled silica nanoparticles for photothermal therapy. *J. Mater. Chem.* **20**, 5182–5185.
- Sharma, P., S. C. Brown, N. Bengtsson, Q. Zhang, G. A. Walter, S. R. Grobmyer, S. Santra, H. Jiang, E. W. Scott and B. M. Moudgil (2008) Gold-speckled multimodal nanoparticles for noninvasive bioimaging. *Chem. Mater.* **20**, 6087–6094.
- Bonnett, R. (2000) *Chemical Aspects of Photodynamic Therapy*. Gordon and Breach Science Publishers, London.
- Hayashi, K., M. Nakamura, H. Miki and S. Ozaki (2014) Photo-stable iodinated silica/porphyrin hybrid nanoparticles with heavy-atom effect for wide-field photodynamic/photothermal therapy using single light source. *Adv. Funct. Mater.* **24**, 503–513.
- Gorman, A., J. Killoran, C. O'Shea, T. Kenna, W. M. Gallagher and D. F. O'Shea (2004) In vitro demonstration of the heavy-atom effect for photodynamic therapy. *J. Am. Chem. Soc.* **126**, 10619–10631.
- De Simone, B. C., G. Mazzone, N. Russo, E. Sicilia and M. Toscano (2017) Metal atom effect on the photophysical properties of Mg(II) Zn(II), Cd(II), and Pd(II) tetraphenylporphyrin complexes proposed as possible drugs in photodynamic therapy. *Molecules* **22**, (7), 1093, 1–10.
- Obirai, J. and T. Nyokong (2005) Synthesis, electrochemical and electrocatalytic behaviour of thiophene-appended cobalt, manganese and zinc phthalocyanine complexes. *Electrochim. Acta* **50**, 5427–5434.
- Ambroz, M., A. Beeby, A. J. McRobert, M. S. C. Simpson, R. K. Svensen and D. Phillips (1991) Preparative, analytical and fluorescence spectroscopic studies of sulphonated aluminium phthalocyanine photosensitizers. *J. Photochem. Photobiol. B: Biol.* **9**, 87–95.
- Dube, E., D. O. Oluwole and T. Nyokong (2017) Photophysical-chemical behaviour of anionic indium phthalocyanine when grafted onto Ag_xAu_y and porous silica nanoparticles. *J. Lumin.* **190**, 353–363.
- Gole, A. and C. J. Murphy (2004) Seed-mediated synthesis of gold nanorods: Role of the size and nature of the seed. *Chem. Mater.* **16**, 3633–3640.
- Mthethwa, T. P., S. Tuncel, M. Durmuş and T. Nyokong (2013) Photophysical and photochemical properties of a novel thiol terminated low symmetry zinc phthalocyanine complex and its gold nanoparticles conjugate. *Dalton Trans.* **42**, 4922–4930.
- Fashina, A., E. Antunes and T. Nyokong (2013) Characterization and photophysical behavior of phthalocyanines when grafted onto silica nanoparticles. *Polyhedron* **53**, 278–285.
- Masilela, N. and T. Nyokong (2013) The interaction of silver nanoparticles with low symmetry cysteinyl metallophthalocyanines and their antimicrobial effect. *J. Photochem. Photobiol. A: Chem.* **255**, 1–9.
- Decker, M., M. W. Klein, M. Wegener and S. Linden (2007) Circular dichroism of planar chiral magnetic metamaterials. *Opt. Lett.* **32**, 856–858.
- Li, L., J. F. Zhao, N. Won, H. Jin, S. Kim and J. Y. Chen (2012) Quantum dot - aluminum phthalocyanine conjugates perform photodynamic reactions to kill cancer cells via fluorescence resonance energy transfer (FRET). *Nanoscale Res. Lett.* **7**, 386–393.
- Fery-Forgues, S. and D. Lavabre (1999) Modified mesoporous silica nanoparticles as a reusable, selective chromogenic sensor for mercury (II) recognition. *J. Chem. Educ.* **76**, 1260–1264.
- Tran-Thi, T. H., C. Desforge, C. Thiec and S. J. Gaspard (1989) Singlet-singlet and triplet-triplet intramolecular transfer processes in a covalently linked porphyrin-phthalocyanine heterodimer. *J. Phys. Chem.* **93**, 1226–1233.
- Ogunsipe, A., J. Y. Chen and T. Nyokong (2004) Photophysical and photochemical studies of zinc (II) phthalocyanine derivatives—effects of substituents and solvents. *New J. Chem.* **28**, 822–827.
- Kuznetsova, N. A., N. S. Gretsova, O. A. Yuzhakova, V. M. Negri-movskii, O. L. Kaliya and E. A. Luk'yanets (2001) New reagents for determination of the quantum efficiency of singlet oxygen generation in aqueous media. *Russ. J. Gen. Chem.* **71**, 36–41.
- Spiller, W., H. Kliesch, D. Wohrle, S. Hackbarth, B. Roder and G. Schnurpfeil (1998) Singlet oxygen quantum yields of different photo-sensitizers in polar solvents and micellar solutions. *J. Porphyrins Phthalocyanines* **2**, 145–158.
- Nyokong, T. and E. Antunes (2010) Photochemical and photophysical properties of metallophthalocyanines. In *The Handbook of Porphyrin Science* (Edited by K. M. Kadish, K. M. Smith and R. Guilard), pp. 247–349. World Scientific, Singapore.
- Mack, J. and M. J. Stillman (2003). *Handbook of Porphyrin and Related Macrocycles*. Vol. **16** (Edited by K. M. Kadish, K. M. Smith and R. Guilard), pp. 43. Academic Press, New York.
- Gurel, E., M. Pişkin, S. Altun, Z. Odabaş and M. Durmuş (2015) Synthesis, characterization and investigation of the photophysical and photochemical properties of highly soluble novel metal-free, zinc(II), and indium(III) phthalocyanines substituted with 2,3,6-trimethylphenoxy moiety. *Dalton Trans.* **44**, 6202–6211.
- Sakamoto, K., E. Ohno-Okumura, T. Kato and H. Soga (2010) Synthesis of near-infrared absorbed metal phthalocyanine with S-aryl groups at non-peripheral positions. *J. Porphyrins Phthalocyanines* **14**, 47–54.
- Mack, J., M. J. Stillman and N. Kobayashi (2007) Application of MCD spectroscopy to porphyrinoids. *Coord. Chem. Rev.* **251**, 429–453.
- Gouterman, M. (1978) Optical spectra and electronic structure of porphyrins and related rings. In *The Porphyrins* (Edited by D. Dolphin), pp. 1–165. Academic Press, New York.

36. Stillman, M. J. and T. Nyokong (1989) *Phthalocyanines: Properties and Applications*, Ch 3 (Edited by C. C. Leznoff and A. B. P. Lever), pp. 134–289. VCH Publishers, New York.
37. Prabakaran, R., R. Kesavamoorthy, G. L. N. Reddy and F. P. Xavier (2002) Structural Investigation of copper phthalocyanine thin films using X-Ray diffraction, Raman scattering and optical absorption measurements. *Phys. Status Solidi* **229**, 1175–1186.
38. Majles, A. M. H., Z. Dehghani, R. Sahraei, A. Daneshfar, Z. Javadi and F. Divsar (2012) Diffraction patterns and nonlinear optical properties of gold nanoparticles. *J. Quant. Spectrosc. Radiat. Transfer* **113**, 366–372.
39. Jenkins, R. and R. L. Snyder (1996) *Introduction to X-ray Diffraction*. Wiley and Sons, New York.
40. DeRosa, M. C. and R. Jcrutchley (2002) Photosensitized singlet oxygen and its applications. *Coord. Chem. Rev.* **233–234**, 351–371.
41. Castano, A. P., T. N. Demidova and M. R. Hamblin (2004) Mechanisms in photodynamic therapy: Part one—photosensitizers, photochemistry and cellular localization. *Photodiagn. Photodyn. Ther.* **1**, 279–293.